



ISTITUTO NAZIONALE DI RICERCA METROLOGICA
Repository Istituzionale

Control of vortex chirality in bi-component magnetic nanodisks

Original

Control of vortex chirality in bi-component magnetic nanodisks / Manzin, Alessandra; Ferrero, Riccardo. - In: APPLIED PHYSICS LETTERS. - ISSN 0003-6951. - 115:4(2019), p. 042402. [10.1063/1.5110274]

Availability:

This version is available at: 11696/61610 since: 2021-02-18T17:50:18Z

Publisher:

AIP

Published

DOI:10.1063/1.5110274

Terms of use:

This article is made available under terms and conditions as specified in the corresponding bibliographic description in the repository

Publisher copyright

(Article begins on next page)

Control of vortex chirality in bi-component magnetic nanodisks

Cite as: Appl. Phys. Lett. **115**, 042402 (2019); <https://doi.org/10.1063/1.5110274>

Submitted: 15 May 2019 . Accepted: 08 July 2019 . Published Online: 25 July 2019

 Alessandra Manzin, and  Riccardo Ferrero



View Online



Export Citation



CrossMark

ARTICLES YOU MAY BE INTERESTED IN

[The design and verification of MuMax3](#)

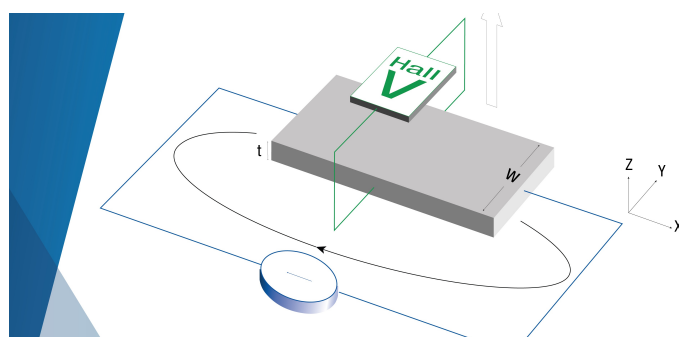
AIP Advances **4**, 107133 (2014); <https://doi.org/10.1063/1.4899186>

[Evolution of magnetic vortex formation in micron-sized disks](#)

Applied Physics Letters **115**, 132407 (2019); <https://doi.org/10.1063/1.5116299>

[Piezo-electrical control of gyration dynamics of magnetic vortices](#)

Applied Physics Letters **115**, 062404 (2019); <https://doi.org/10.1063/1.5110169>



**Tips for minimizing
Hall measurement errors**

Download the Technical Note

 **Lake Shore**
CRYOTRONICS

Control of vortex chirality in bi-component magnetic nanodisks

Cite as: Appl. Phys. Lett. **115**, 042402 (2019); doi: [10.1063/1.5110274](https://doi.org/10.1063/1.5110274)

Submitted: 15 May 2019 · Accepted: 8 July 2019 ·

Published Online: 25 July 2019



View Online



Export Citation



CrossMark

Alessandra Manzin^{1,a)}  and Riccardo Ferrero^{1,2} 

AFFILIATIONS

¹Istituto Nazionale di Ricerca Metrologica (INRIM), Strada delle Cacce 91, 10135 Torino, Italy

²Politecnico di Torino, Corso Duca degli Abruzzi 24, 10129 Torino, Italy

^{a)}Author to whom correspondence should be addressed: a.manzin@inrim.it. Tel.: +39-011-3919825.

ABSTRACT

In the last decade, special attention has been paid to the nucleation and control of the vortex state in magnetic nanostructures, for possible applications in nonvolatile magnetic random access memories and logic networks. Here, we study bicomponent magnetic nanodisks, in both single and 2D array arrangements, as potential storage systems where the information unit is represented by vortex chirality (magnetization rotational direction). We mainly focus on 300 nm diameter disks made of a permalloy lens and an iron crescent, with variable locations of the permalloy-iron interface. Through an extensive micromagnetic modeling analysis, we demonstrate the possibility of tuning, via the application of a magnetic field parallel to the interface, the nucleation of the vortex (always occurring in the permalloy region), its motion up to the expulsion site, and its chirality. Moreover, we find that the vortex stability is preserved over a wide field range also for strongly packed disks, due to the reduced effects of interdisk magnetostatic coupling. The main features of the magnetization reversal mechanism are preserved by reducing the disk diameter up to about 60 nm, making possible their exploitation in concept devices for magnetic encoding and logic computation.

Published under license by AIP Publishing. <https://doi.org/10.1063/1.5110274>

The continuous progress in nanolithography techniques has led to the fabrication of magnetic nanostructures with increasingly complex patterning and lower dimensions for future applications in advanced sensor technologies, magnetologic devices, and high density storage media.^{1,2} In this framework, the nucleation of the vortex state in magnetic nanodisks is a topic of intensive research, due to its possible implementation in data storage and, specifically, in nonvolatile magnetic random access memories. Two units of information can be stored in a single nanodisk, exploiting either vortex polarity (up/down orientation of magnetization in the vortex core) or chirality (clockwise/counterclockwise rotational direction of magnetization).³

Despite the technological potentiality of magnetic vortices, the control of their topological properties still remains a challenging issue.⁴ Different solutions based on broken rotational symmetry were proposed to tailor vortex chirality and possibly polarity, like the use of asymmetric dots with a flattened edge⁵⁻⁷ or regular polygonal nanomagnets with an odd number of sides.⁸⁻¹⁰ Alternatively, “Pac-Man”-like nanodots can be considered to obtain specific chirality and polarity states without the application of out-of-plane magnetic fields for setting polarity.¹¹

Recently, the simultaneous definition of chirality and polarity was achieved in nanodots with a modulated or tapered thickness, by simply changing the in-plane applied field direction.^{12,13} Thickness-modulated disks in the form of a permalloy lens on top of a disk made of the same material were also proposed to control the vortex core location and chirality depending on the magnetostatic interactions between the two regions.¹⁴ At the same time, static and dynamic control of both polarity and chirality was demonstrated for a vortex confined in a magnetic tunnel junction by using resonant excitation with an rf current.¹⁵ Both ac exciting currents, applied in the disk plane, and weak magnetic field pulses were previously proposed as low-energy consumption means to drive vortex-core switching.¹⁶⁻¹⁹

Broken symmetry can also be achieved by means of bicomponent disks (made of two magnetic materials); as an example, angle deposition and lift-off processes were employed to fabricate bicomponent dots consisting of a crescent of iron and a lens of permalloy.²⁰ Their hysteresis loop is characterized by a three-step switching, corresponding to magnetization switching in permalloy lens and to vortex nucleation and expulsion in iron crescent, respectively. This result opens up the possibility of finely controlling the vortex core position, by simply varying the relative dimensions of the two magnetic regions.

In this paper, we investigate bicomponent magnetic nanodisks with a geometrical configuration similar to the one proposed by Shimon *et al.*,²⁰ to explore the possibility of tuning the chirality and stability of the vortex, as well as its nucleation and expulsion, by means of the local shape anisotropies at the two-material interface. The analysis is performed from a micromagnetic numerical point of view, calculating the static hysteresis loops of disks arranged in both single and 2D array configurations. The latter case is considered to study the effects of the magnetostatic interactions between disks on vortex stability.

The simulations are performed by using a parallelized micromagnetic code designed to solve the Landau-Lifshitz-Gilbert equation in samples with complex patterning.²¹ The code implements a norm-conserving scheme based on the Cayley transform and classic Heun method for the magnetization update.^{22,23} The exchange field is calculated by means of a finite difference technique for nonstructured meshes,²⁴ thus allowing the accurate treatment of curvatures without the imposition of boundary corrections.²⁵ This approach enables us to avoid staircase approximation, similarly to finite element^{26–28} and mimetic finite difference techniques.²⁹ For the 2D arrays, periodic boundary conditions are introduced on the edges of the array unit cell.³⁰

The numerical analysis focuses on 20 nm thick disks with diameter $d = 300$ nm and composed of two magnetic regions, i.e., a lens of permalloy (saturation magnetization M_S of 860 kA/m, exchange constant k_{ex} of 13 pJ/m, and negligible magnetocrystalline anisotropy) and a crescent of iron ($M_S = 1700$ kA/m, $k_{ex} = 21$ pJ/m, and cubic magnetocrystalline anisotropy with constant equal to 48 kJ/m³). The reversal mechanism is studied for different fractions of the two constituents, by shifting the position of the permalloy-iron interface. In particular, we vary parameter w , which corresponds to the distance between the interface and the disk left boundary, from 60 nm to 240 nm [inset of Fig. 1(a)]. The interface exchange coupling is treated by introducing a 3 nm thick interlayer between the two magnetic regions, with averaged properties (harmonic means of saturation magnetization and exchange constant values).

To guarantee the accurate reconstruction of the disk curved boundaries and interface, we use a nonstructured mesh made of hexahedra with an average size of 3.5 nm. The equilibrium points along the hysteresis loops are calculated by fixing damping coefficient α to 0.1. In this way, the convergence to magnetization equilibrium

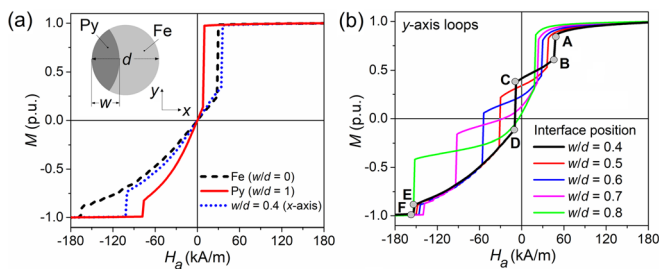


FIG. 1. (a) Hysteresis loop descending branches of single homogeneous permalloy and iron disks, compared to the x-axis loop of a bicomponent disk with $w/d = 0.4$. Inset: Schematic of the bicomponent disk composed of a lens of permalloy, with thickness w , and a crescent of iron. (b) Descending branches of y-axis hysteresis loops vs w/d . Magnetization is normalized to saturation value.

configurations is accelerated and, thanks to the Cayley transform based time-integration scheme, we can use quite large time steps (500 fs) with no risks of numerical instabilities.³¹ The convergence to an equilibrium point is verified when the maximum value of the local misalignment between magnetization and the effective field, $|\mathbf{M}(\mathbf{r}) \times \mathbf{H}_{eff}(\mathbf{r})|/M_S^2(\mathbf{r})$, is lower than a predetermined threshold, here fixed to 10^{-8} .

The single bicomponent disks are characterized by a strong shape anisotropy, as demonstrated by the differences in the descending branches of the hysteresis loops calculated for different values of parameter w along the directions orthogonal (x -axis) and parallel (y -axis) to the interface. The x -axis loops are similar to the ones of the homogeneous disks, with two irreversible jumps corresponding to vortex nucleation and expulsion, connected through a reversible part dominated by a vortex shift along the vertical direction. At remanence, a negligible average magnetization is always found [Fig. 1(a)]. As shown in Fig. 1(b), the y -axis loops are generally characterized by three irreversible jumps; the magnetization configurations immediately before and after the jumps are reported in Fig. 2(a) for $w/d = 0.7$. The first jump (from equilibrium point #A to #B) corresponds to evolution from the C-state to vortex nucleation in permalloy lens. Between the first and second irreversible jumps (from #B to #C), the vortex moves reversibly along the x -axis up to the interface. The second jump (from #C to #D) is associated with vortex horizontal motion from the interface to a point in the iron crescent. Between the second and third irreversible jumps (from #D to #E), the vortex moves reversibly along the x -axis up to a position closer to the disk right boundary. The third jump (from #E to #F) corresponds to vortex expulsion, occurring always in the iron region. When $w/d = 0.8$, the magnetization reversal is characterized by only two irreversible jumps, with the second jump directly associated with evolution from the vortex anchored to the interface to vortex expulsion; equilibrium points #D and #E are not present.

As illustrated in Fig. 2(b), for the y -axis loops, the spatial position u of the vortex at equilibrium points #B, #C, #D, and #E is a function of parameter w , coinciding with w for point #C. For point #B, there is a linear dependence on w up to $w/d = 0.6$, reaching a plateau for larger values; for point #D, the linear dependence extends up to $w/d = 0.7$, and for point #E, u is nearly constant, on the order of 0.96 d . It results that for the reversal mechanism along the y -axis, it is possible to

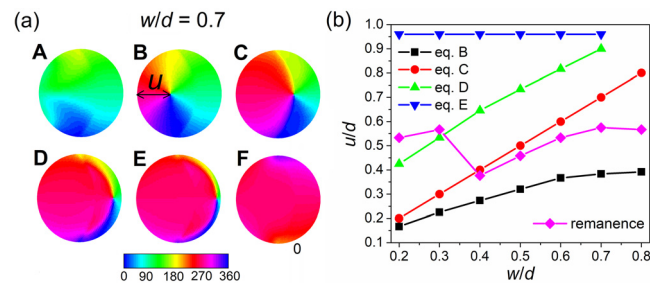


FIG. 2. (a) Equilibrium magnetization configurations along the y-axis hysteresis loop descending branch [Fig. 1(b)], for $w/d = 0.7$. The color bar represents the angle, in degrees, between the magnetization vector and the x-axis. (b) Vortex spatial position (u/d) vs w/d for the remanence state and equilibrium points #B, #C, #D, and #E. Parameter u describes the distance of the vortex core from the disk left boundary.

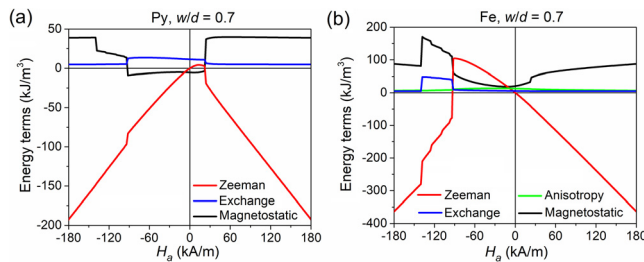


FIG. 3. Zeeman, exchange, magnetostatic, and anisotropy (when present) energy densities vs applied field for (a) permalloy lens and (b) iron crescent, calculated for $w/d = 0.7$. The energy term evolution is evaluated along the y -axis loop descending branch.

monitor the vortex position and control both vortex nucleation and expulsion, which occur in permalloy lens and at the opposite iron boundary, respectively.

The reason why the vortex nucleates first in permalloy lens and then evolves with a stepped motion with well-defined positions can be understood by analyzing the energy density terms vs the applied field, separately calculated for the two magnetic regions (Fig. 3 for $w/d = 0.7$). Before the first irreversible jump, the magnetization curls forming a C-state, which will govern the chirality of the successive vortex. In particular, the magnetization mainly curls in the permalloy lens and rotates internally following the interface curvature: this will always lead to a counterclockwise (CCW) chirality when the field is swept from positive to negative values and to a clockwise (CW) chirality for the opposite hysteresis loop branch. The C-state formation is accompanied by a reduction in magnetostatic energy in the iron crescent and in a slight increase in the same energy term in the permalloy lens, due to the generation of magnetic poles along the disk left boundary. Magnetic poles appear at the interface at the same time (Fig. S1 in the [supplementary material](#)). Vortex nucleation during the first irreversible jump leads to a strong reduction in magnetostatic energy in permalloy lens, thanks to the disappearance of the lateral magnetic poles. At the irreversible jump end (#B), the vortex locates internally to permalloy lens at a position that enables us to reduce as much as possible the magnetostatic volume integral. Magnetostatic energy decreases also in the iron region, due to the greater curling of magnetization caused by vortex closure. Finally, the vortex formation is accompanied by a steep increase in exchange and Zeeman energies in permalloy lens.

Between the first and second irreversible jumps, there is a weak reduction in magnetostatic energy in permalloy, since the vortex motion toward the interface contributes to a greater alignment of magnetization with the magnetostatic field. At the end of the second irreversible jump (#D), magnetization reversal in permalloy is completed. This leads to an increment of the relative magnetostatic energy, since the magnetostatic field and magnetization become antiparallel, and to a decrease in exchange energy. In the iron crescent, magnetostatic energy increases, compensated by Zeeman energy reduction, if $w/d > 0.5$, due to strong vortex compression, while decreases if $w/d \leq 0.5$, due to vortex anchorage to a position that allows the magnetostatic volume integral minimization. At the same time, there is a rise in exchange energy.

Between the second and third irreversible jumps, magnetostatic energy increases in both permalloy and iron regions, since with vortex

motion toward the disk right boundary, there is an enlargement of the areas where magnetization and the magnetostatic field are antiparallel. At the end of the third irreversible jump (#F), the C-state forms again, leading to an increment of magnetostatic energy in permalloy lens, due to magnetic pole generation, and to a reduction in the same energy term in iron, consequently to a greater magnetization curling.

It is interesting to point out that for disks with exchanged features (lens in iron and crescent in permalloy), the vortex shows a CW chirality when the field is swept from positive to negative values and a CCW chirality for the opposite hysteresis loop branch (schematic in Fig. S2 of the [supplementary material](#)). Vortex chirality is driven again by the previous C-state configuration, which mainly curls in the permalloy region and follows internally the interface shape (Fig. S3 in the [supplementary material](#)). Also in this case, the C-state governs the formation site of the vortex, which appears always in permalloy and then moves toward the iron region.

As illustrated in Fig. 1(b), for the disks with permalloy lens and iron crescent, the shape of the y -axis loops is strongly influenced by parameter w , whose variation leads to a modulation of the applied field range between vortex nucleation and expulsion, thus affecting vortex stability. Possible variations in the magnetization reversal mechanism can be induced by microstructural defects or material impurities. To investigate this effect, we perform a set of simulations introducing a variable number of randomly distributed nanoscale defects, assumed to be nonmagnetic regions with size Δv around 5 nm or 10 nm [some results are reported in Fig. 4(a) for $w/d = 0.5$]. We observed that the defects with $\Delta v \approx 5$ nm weakly affect magnetization reversal, with a slight change in the hysteresis loop shape. In particular, the defects closest to the disk diameter parallel to the x -axis act as pinning sites for the vortex, which moves orthogonally to the interface from permalloy to iron. This results in the addition of intermediate irreversible jumps characterized by a small variation in the average magnetization. Stronger pinning effects with a more appreciable change in loop shape can be found for highly concentrated 10 nm size defects. In this case, there is the appearance of several steps along the loop branches, due to the more probable anchorage of the vortex to multiple sites, as illustrated by the magnetization configuration maps in Fig. 4(a). Anyway, the main features of the reversal mechanism observed in nondefective disks are preserved, like the control of vortex chirality, the remanence magnetization configuration, and the vortex displacement from permalloy to iron regions. Moreover, the applied field interval between vortex nucleation and expulsion and the field value at which the vortex pins at the interface are weakly affected, also for high defect concentrations.

A detriment of vortex stability may be encountered when arranging the disks in 2D arrays, as a consequence of the interdisk magnetostatic coupling, which can influence the vortex formation process.^{32,33} To analyze this effect, we have calculated the y -axis loops of strongly packed arrays of nondefective disks [inset of Fig. 4(b)], with a spacing s (distance between boundaries) equal to 30 nm and 50 nm. Some of the results obtained for $s = 30$ nm are shown in Fig. 4(b), which reports the hysteresis loops of 2D arrays of both homogeneous disks and bicomponent disks with $w/d = 0.5$. The simulations are performed under the assumption of the same vortex chirality-polarity configuration³⁴ for the interacting disks, due to the use of periodic boundary conditions.

It is worth noting that also for very high density, the loop shape of bicomponent disk arrays is slightly altered with respect to the single

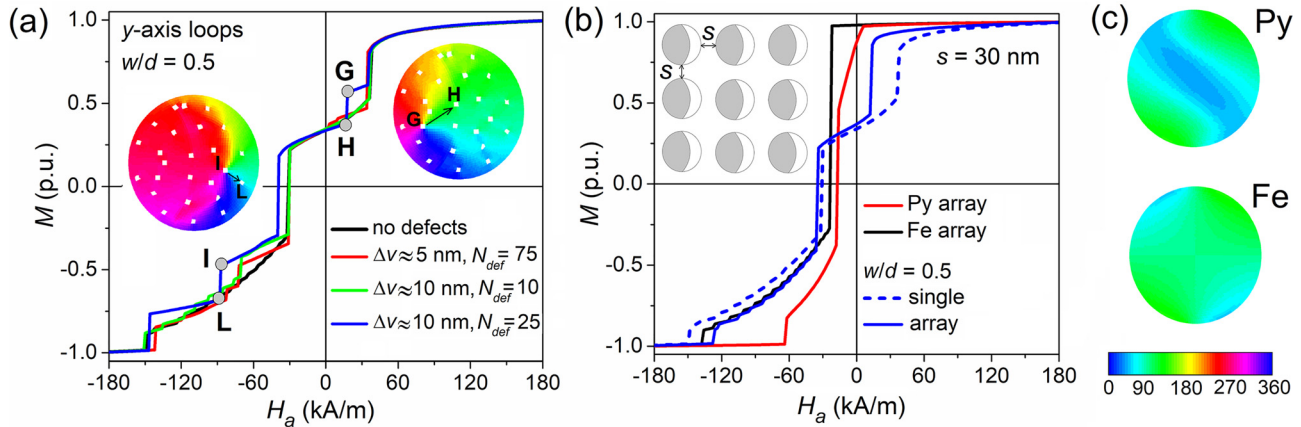


FIG. 4. (a) Descending branches of γ -axis hysteresis loops of bicomponent disks ($w/d = 0.5$), with a number N_{def} of randomly distributed defects (size Δv around 5 nm or 10 nm). The magnetization maps ($\Delta v \approx 10$ nm and $N_{def} = 25$) illustrate defect pinning role. (b) Influence of magnetostatic coupling on 2D array hysteresis loops, for a spacing s of 30 nm; the graph compares the results obtained for homogeneous and bicomponent disks with $w/d = 0.5$. In the loops in (a) and (b), magnetization is normalized to saturation value. (c) Remanence state for highly packed homogeneous disks ($s = 30$ nm) made of permalloy (top) and iron (bottom). The color bar [for maps in (a) and (c)] represents the angle, in degrees, between the magnetization vector and the x-axis.

disk case, while a significant change is found for homogeneous disks. For both permalloy and iron disk arrays, vortex nucleation is strongly delayed and remanence is no more characterized by the vortex configuration, but by the S-state, as depicted in Fig. 4(c). The reason is that for homogeneous disks, the magnetostatic field is more intense and the stray field lines from a disk cross a large external area, investing an extended portion of neighboring disks. This leads to a local alteration of the effective field, with a consequent modification of the energy landscape in the neighboring disks.

For bicomponent disks, the particular C-state that forms before vortex nucleation gives rise to a more confined stray field, generated by the two magnetic poles along the permalloy side boundary. As a consequence, the stray field produced by a disk invests a smaller portion of the external area, where the other disks are located, resulting in a weak magnetostatic coupling. The role of the C-state in driving a stable vortex state can be explained by comparing the magnetostatic interaction energies along the reversal process of homogeneous and bicomponent disk arrays (Fig. S4 in the supplementary material). In particular, a strong reduction in the interaction energy can be observed in bicomponent disks during the formation of the C-state that anticipates vortex nucleation (from saturation to the first irreversible jump). Moreover, for bicomponent disks, the state with vortex pinned at the interface leads to a zero magnetostatic coupling.

The dependence of remanent magnetization on parameter w is shown in Fig. 5(a), which compares the results obtained with single disks to the ones found for the 2D arrays. When $s = 50$ nm, the vortex state is preserved for w/d ranging between 0.2 and 0.7, while this interval reduces to 0.4–0.6 when $s = 30$ nm. Advantageously, in both these ranges, the remanent magnetization values are practically coincident with the ones found for the single disks. The above result is accompanied by a high vortex stability, as demonstrated in Fig. 5(b), which illustrates the influence of w and s on vortex nucleation and expulsion fields and on the amplitude ΔH of the field interval between vortex nucleation and expulsion. In particular, when $w/d = 0.4$ –0.6, the reduction in s has a moderate effect on ΔH , which is characterized by

a quite small decrease, i.e., around 25% (20%) for $s = 30$ nm (50 nm). Overall, for the 2D arrays, the greatest value of ΔH is obtained with $w/d = 0.4$, the condition for which the vortex remanence state is preserved also for high packing densities. Additionally, for $w/d = 0.8$, the 2D array arrangement has a weak influence on the vortex expulsion field, since the vortex is directly expelled from the interface, resulting in a low stray field and thus in a small magnetostatic coupling.

Finally, we investigate the possibility of lowering the size of the bicomponent disks while preserving the main features of the magnetization reversal process, i.e., three-step switching, control of vortex chirality, and high vortex stability. We found that the above properties can be guaranteed by reducing the diameter up to ~ 60 nm for a thickness of 20 nm (Fig. S5 in the supplementary material). For this size, the switching mechanism in homogeneous permalloy disks is coherent rotation, while homogeneous iron disks present the vortex state.³⁵ The combination of the two materials gives rise to the three-step switching as observed in the larger dimension disks. Moreover, for the 60 nm bicomponent disks with $w/d = 0.5$, vortex stability is preserved also in

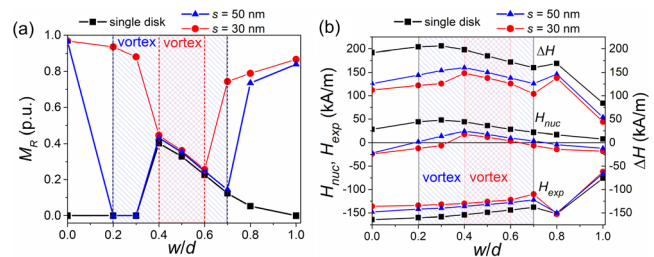


FIG. 5. (a) Influence of parameter w and interdisk spacing s on the remanent magnetization, normalized to saturation value. (b) Influence of w and s on vortex nucleation field H_{nuc} , vortex expulsion field H_{exp} , and amplitude ΔH of the field interval between nucleation and expulsion. The two graphs compare the results obtained for single disks to the ones of 2D arrays with s equal to 30 and 50 nm. The stripe patterned rectangles identify the intervals of variation of w where the vortex state is preserved at remanence.

highly packed 2D arrays, where spacing s is around 30 nm. All these results make 60 nm size bicomponent disks competitive with the recently proposed concept devices for encoding or magnetologic networks based on skyrmions or chiral bobbers.^{36,37}

Regarding the potential application in memories with information stored in chirality, the stable vortex state observed at remanence could be selectively switched by applying localized in-plane magnetic field pulses and detected by magnetoresistive effects.^{3,13,38,39} Thanks to the two-material interface, which permits us to obtain a quasicomplete flux-closure that minimizes magnetostatic coupling, the bicomponent disks can be strongly packed together, leading to high storage density. Another advantage regards the possibility of monitoring the vortex pinning, depinning, and position inside the disks through the intermediate irreversible jump and the associated anchorage to the interface, useful features for the development of magnetoelectronic devices.

See the [supplementary material](#) for maps of the magnetostatic field in bicomponent disks, vortex chirality as a function of disk structure, reversal process of disks with iron lens and permalloy crescent, evolution of magnetostatic interaction energies, and hysteresis loops of 60 nm size disks.

REFERENCES

- ¹J. W. Lau and J. M. Shaw, *J. Phys. D: Appl. Phys.* **44**, 303001 (2011).
- ²J. M. De Teresa, A. Fernández-Pacheco, R. Córdoba, L. Serrano-Ramón, S. Sangiao, and M. R. Ibarra, *J. Phys. D: Appl. Phys.* **49**, 243003 (2016).
- ³R. Hertel, *Nat. Nanotechnol.* **8**, 318–320 (2013).
- ⁴Y. Zheng and W. J. Chen, *Rep. Prog. Phys.* **80**, 086501 (2017).
- ⁵R. K. Dumas, D. A. Gilbert, N. Eibagi, and K. Liu, *Phys. Rev. B* **83**, 060415(R) (2011).
- ⁶M. Schneider, H. Hoffmann, and J. Zweck, *Appl. Phys. Lett.* **79**, 3113–3115 (2001).
- ⁷T. Kimura, Y. Otani, H. Masaki, T. Ishida, R. Antos, and J. Shibata, *Appl. Phys. Lett.* **90**, 132501 (2007).
- ⁸M. Jaafar, R. Yanes, D. Perez de Lara, O. Chubykalo-Fesenko, A. Asenjo, E. M. Gonzalez, J. V. Anguita, M. Vazquez, and J. L. Vicent, *Phys. Rev. B* **81**, 054439 (2010).
- ⁹S. Yakata, M. Miyata, S. Nonoguchi, H. Wada, and T. Kimura, *Appl. Phys. Lett.* **97**, 222503 (2010).
- ¹⁰Y. Wen, Z. Feng, B. F. Miao, R. X. Cao, L. Sun, B. You, D. Wu, W. Zhang, Z. S. Jiang, R. Cheng, and H. F. Ding, *J. Magn. Magn. Mater.* **370**, 68–75 (2014).
- ¹¹V. Cambel and G. Karapetrov, *Phys. Rev. B* **84**, 014424 (2011).
- ¹²S. Agramunt-Puig, N. Del-Valle, C. Navau, and A. Sanchez, *Appl. Phys. Lett.* **104**, 012407 (2014).
- ¹³V. Uhlir, M. Urbánek, L. Hladík, J. Spousta, M.-Y. Im, P. Fischer, N. Eibagi, J. J. Kan, E. E. Fullerton, and T. Šikola, *Nat. Nanotechnol.* **8**, 341–346 (2013).
- ¹⁴G. Shimon, A. O. Adeyeye, and C. A. Ross, *Phys. Rev. B* **87**, 214422 (2013).
- ¹⁵A. S. Jenkins, E. Grimaldi, P. Bortolotti, R. Lebrun, H. Kubota, K. Yakushiji, A. Fukushima, G. de Loubens, O. Klein, S. Yuasa, and V. Cros, *Appl. Phys. Lett.* **105**, 172403 (2014).
- ¹⁶Y. Liu, S. Gliga, R. Hertel, and C. M. Schneider, *Appl. Phys. Lett.* **91**, 112501 (2007).
- ¹⁷K. Yamada, S. Kasai, Y. Nakatani, K. Kobayashi, H. Kohno, A. Thiaville, and T. Ono, *Nat. Mater.* **6**, 270–273 (2007).
- ¹⁸B. Van Waeyenberge, A. Puzic, H. Stoll, K. W. Chou, T. Tylliszczak, R. Hertel, M. Fähnle, H. Brückl, K. Rott, G. Reiss, I. Neudecker, D. Weiss, C. H. Back, and G. Schütz, *Nature* **444**, 461–464 (2006).
- ¹⁹R. Hertel, S. Gliga, M. Fähnle, and C. M. Schneider, *Phys. Rev. Lett.* **98**, 117201 (2007).
- ²⁰G. Shimon, A. O. Adeyeye, and C. A. Ross, *Appl. Phys. Lett.* **101**, 083112 (2012).
- ²¹O. Bottauscio and A. Manzin, *J. Appl. Phys.* **115**, 17D122 (2014).
- ²²O. Bottauscio and A. Manzin, *IEEE Trans. Magn.* **47**, 1154–1157 (2011).
- ²³D. Lewis and N. Nigam, *J. Comput. Appl. Math.* **151**, 141–170 (2003).
- ²⁴O. Bottauscio and A. Manzin, *IEEE Trans. Magn.* **48**, 3250–3253 (2012).
- ²⁵C. J. García-Cervera, Z. Gimbutas, and E. Weinan, *J. Comput. Phys.* **184**, 37–52 (2003).
- ²⁶W. Scholz, J. Fidler, T. Schrefl, D. Suess, R. Dittrich, H. Forster, and V. Tsiantos, *Comput. Mater. Sci.* **28**, 366–383 (2003).
- ²⁷A. Kákay, E. Westphal, and R. Hertel, *IEEE Trans. Magn.* **46**, 2303–2306 (2010).
- ²⁸E. Kritisikis, A. Vaysset, L. D. Buda-Prejbeanu, F. Alouges, and J.-C. Toussaint, *J. Comput. Phys.* **256**, 357–366 (2014).
- ²⁹E. Kimb and K. Lipnikov, *J. Comput. Phys.* **328**, 109–130 (2017).
- ³⁰A. Manzin and O. Bottauscio, *J. Phys. D: Appl. Phys.* **45**, 095001 (2012).
- ³¹A. Manzin and O. Bottauscio, *J. Appl. Phys.* **108**, 093917 (2010).
- ³²B. Van de Wiele, S. Fin, A. Sarella, P. Vavassori, and D. Biserio, *Appl. Phys. Lett.* **105**, 162407 (2014).
- ³³R. Ferrero, A. Manzin, G. Barrera, F. Celegato, M. Coisson, and P. Tiberto, *Sci. Rep.* **9**, 6591 (2019).
- ³⁴Y. Lu, Z. Zhang, and Y. Liu, *J. Appl. Phys.* **109**, 103906 (2011).
- ³⁵J. Mejía-López, D. Altbir, P. Landeros, J. Escrig, A. H. Romero, I. V. Roshchin, C.-P. Li, M. R. Fitzsimmons, X. Battle, and I. K. Schuller, *Phys. Rev. B* **81**, 184417 (2010).
- ³⁶F. Zheng, F. N. Rybakov, A. B. Borisov, D. Song, S. Wang, Z.-A. Li, H. Du, N. S. Kiselev, J. Caron, A. Kovács, M. Tian, Y. Zhang, S. Blügel, and R. E. Dunin-Borkowski, *Nat. Nanotechnol.* **13**, 451–455 (2018).
- ³⁷A. Fert, N. Reyren, and V. Cros, *Nat. Rev. Mater.* **2**, 17031 (2017).
- ³⁸V. Sluka, A. Kákay, A. M. Deac, D. E. Bürgler, C. M. Schneider, and R. Hertel, *Nat. Commun.* **6**, 6409 (2015).
- ³⁹H. Vigo-Cotrina and A. P. Guimarães, *J. Magn. Magn. Mater.* **460**, 160–164 (2018).